ORIGINAL ARTICLE

Effect of the Air Duct System of a Simplified Vehicle Model on Aerodynamic Performance

Alemayehu W. Huluka[1] and Chul-Ho Kim[2*]

[1]Department of Automotive Engineering, Graduate School, Seoul National University of Science & Technology, 232 Gongneung-ro, Nowon-gu, Seoul 01811, Korea
[2]Department of Mechanical & Automotive Engineering, Seoul National University of Science & Technology, 232 Gongneung-ro, Nowon-gu, Seoul 01811, Korea
Phone: +821052196304; Fax: +8229797032

ABSTRACT – In this numerical study, ducted and flipped Ahmed model is used to study aerodynamic characteristics of ducted models and how ducting would contribute to the energy consumption reduction effort from aerodynamic resistance. Three-dimensional, incompressible, and steady governing equations were solved by commercial software PHOENICS (version 2018) with extended k-ε turbulent model proposed by Chen-Kim (1987). The study can be considered as a steppingstone to bring a new approach to design aerodynamically efficient vehicle by ducting target vehicles. To investigate the feasibility of the ducting for aerodynamic energy efficiency improvement, fundamental study has been conducted numerically on a simple body before applying to appropriate vehicle model. It is observed from the study that ducting a cross-sectional area of 9.6% of a model would reduce over 19% of the pressure drag at a speed of 100km/h, to the contrary the increase in skin friction drag is noted although its significance to the total drag is very less compared to pressure drag. Therefore, study of air duct and its effect on aerodynamic performance is expected to contribute to improvement of electric vehicle aerodynamic performance.

INTRODUCTION

Automobile aerodynamic design has been given attention since 1970's fuel price inflation [1, 2]. Since then, many efforts have been made to improve vehicle energy efficiency by reducing aerodynamic resistance. Several types of drag reduction technologies have been utilised or suggested to reduce drag. These include surface shaping for attached flow, surface shaping for separated flow, surface motion, surface permeability, mass addition and energising the external flow [1]. For more details on the drag reduction technologies, the following literature and the references therein are suggested among several others [3-8]. Some of these literature broadly classify these drag reduction technologies as passive, active and reactive flow control techniques. Some of the techniques find their wide application in marine and air vehicles where friction drag is significant. Most of the studies conducted and the practical methods used so far on ground vehicle aerodynamics were mainly focused on external drag reduction technique, particularly using surface shaping. Along with the aerodynamic shape design, the study of external fluid flow over the automobile body has got a major focus until date [2-8].

Among resistance forces acting on a moving vehicle, aerodynamic resistance is the dominant one at higher vehicle speeds. Much of the power driving the vehicle is expending to overcome the air resistance [9 -12]. Aerodynamic drag typically accounts over 65% of the total resistance for the medium sized car at 100 km/h [9 -13]. Hence, reducing drag contributes significantly to the fuel economy of a car and the reduction of carbon emission for petroleum-based vehicles [2, 14]. Synonymously to save battery energy for battery electric vehicle.

The emerging electric car technology is good news for emission reduction. Almost every car industry is developing or has a plan to develop electric car, hoping that it will be a future car. But the driving range per charge remains a challenge to the industry. This study is seeking for alternative and supplementing engineering solution to ongoing electric vehicle driving range extension. Dedicated to investigating the possible opportunity to maximise the aerodynamic performance of the electric vehicle by conducting a fundamental and preliminary study related to front panel configuration and ducting effect as usually the front end of electric vehicles is closed. The intension of this study is not only to reduce drag but also to extract aerodynamic flow energy through the duct without significant change on the vehicle drag. But before discussing details of the energy harvesting mechanisms and its feasibility, fundamental studies are needed. This fundamental study gives insight into the possibility or feasibility of the drag reduction option, including the energy harvesting concept. In this regard, ducting and its flow characteristic is discussed in this paper based on the numerical experiment.

ROAD-LOAD POWER OF VEHICLE

The road-load power(P_{rl}) of a moving vehicle is composed of the rolling resistance, aerodynamic resistance, gradient resistance and acceleration resistance and the general form of the governing equation is expressed as [15]:

$$P_{rl} = P_{roll} + P_{aero} + P_{grad} + P_{acc} \tag{1}$$

$$P_{rl} = \left(M_v \mathrm{g}\, f_r V\cos\theta + C_D \frac{1}{2}\rho_a A_f V^3 + M_v \mathrm{g}V\sin\theta + M_v \delta V \frac{dV}{dt} \right) \tag{2}$$

where M_v is mass of vehicle, f_r is rolling resistance coefficient, θ is gradient of road, ρ_a is air density, C_D is drag coefficient of vehicle and δ is mass factor. At high-speed driving condition, the power needed to overcome aerodynamic resistance is extremely significant and is proportional to triple times of the vehicle speed.

Aerodynamic resistance D consists of pressure resistance (D_P) and skin friction resistance (D_f). Aircraft and water vehicle drag is comprised of a significant amount of both pressure and skin-friction drag. But ground vehicle aerodynamic resistance is dominated by pressure drag. On ground vehicle drag, the stagnation pressure acting on the front face of a vehicle and rear induced drag takes the major contribution to the total aerodynamic resistance than the skin friction on the surface of the vehicle[1-3, 8].

$$D = D_p + D_f \tag{3}$$

where the pressure drag D_p may divide into the profile pressure drag at the front side and the induced pressure drag at the rear side of the vehicle.

DESCRIPTION OF TEST VEHICLE MODEL

Aerodynamic research of road vehicles often employs a simplified vehicle model, such as MIRA, Ahmed body, SAE body, and several other standard models to gain general insights. These simplified models offer the advantage of a reasonable computational and experimental effort compared to real vehicles and the possibility to examine the flow effects of different parts of the vehicle with limited interference effects. Therefore, such models are well suited for validation purposes [16]. Five (4:1) scaled modified Ahmed models [17] with dimension 4.176m x 1.556m x 1.152m (Lo x W x H) are used in this study. One is a base model with no duct and four of them are ducted with different duct size. Rectangular duct is proposed for this study and the lower surface of the duct is fixed at a constant height from the lower surface of the model. The detail specification of each model vehicle is in Table 1, Figure 1 and Figure 2.

In previous studies including [17], the standard Ahmed model is frequently used for vehicle aerodynamic studies with special focus on the effects of the rear slant angle on the rear flow structure and drag force. In this study, the model is deliberately reverse oriented taking van's shape for the sake of duct flow study and convenience for ducting as the basic car body flow characteristic remains same.

Table 1. Specification of the model vehicles.

Model code	Cross-sectional area of air duct($H`{\times}W`$)	Area ratio*
M0	Base model with no duct	0%
M1	Model with $(1072{\times}160)$ mm^2 duct	9.6%
M2	Model with $(1072{\times}240)$ mm^2 duct	14.4%
M3	Model with $(1072{\times}320)$ mm^2 duct	19.1%
M4	Model with $(1072{\times}400)$ mm^2 duct	23.9%

*Area Ratio (RA); $RA = A_d / A_f$ where A_f is the frontal projected area of the base model and A_d is the cross-sectional area of the duct ($A_d = H`\mathrm{x}W`$)
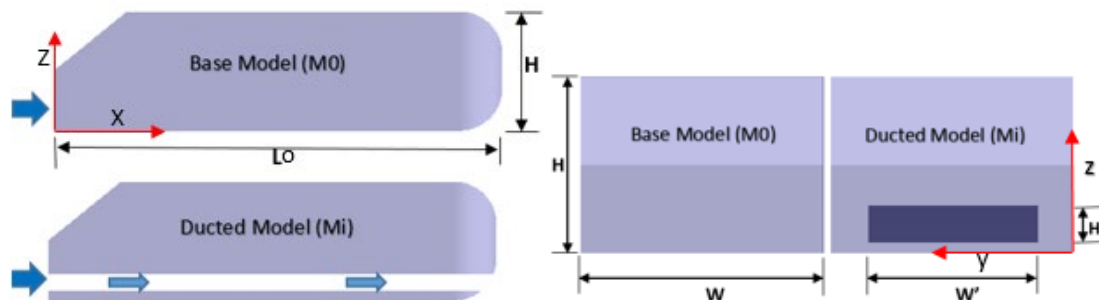

Figure 1. Side and front view of the model vehicles.

Ducted models are with and without front chamfer for evaluation of duct flow phenomena as indicated in Figure 2. The chamfered ducts used an elliptic arc (quarter arc of an ellipse with a semi-major axis (a) = 1000 mm and semi-minor axis (b) = 90 mm) with a major axis along duct length in all duct front edges and tested for comparative analysis.
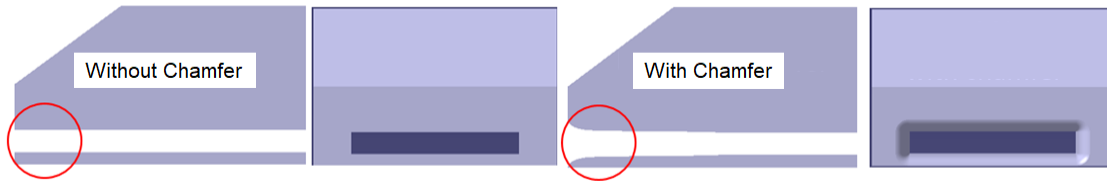

Figure 2. Air duct with and without the front chamfer.

NUMERICAL SCHEME AND BOUNDARY CONDITIONS

In this study, the Finite Volume Method (FVM) was used to perform the numerical calculation for the model vehicles without the side wind. Therefore, the airflow field of the control volume is reasonably assumed to be steady-state, incompressible and turbulent 3D flow field. The general-purpose CFD code, PHOENICS (ver.2018) was used for a numerical calculation of the turbulent incompressible flow field. 3D Naiver-Stokes equations were solved with KECHEN turbulent model (Chen-Kim κ-ε model) which is the modified standard κ-ε turbulent model. Turbulent boundary layer with no-slip condition near the solid surface was modelled by log law.

Chen-Kim κ-ε model believed to improve the dynamic response of the Epsilon equation by introducing an additional time scale and source term. In addition, several of the standard-model coefficients are adjusted so that the model maintains a good agreement with experimental data on classical turbulent shear layers [18]. Therefore, the main reason for the choice of the Chen-Kim modified (k-ε) version in this study was its ability proven to perform better in both no equilibrium and separated flows [18]. The numerical domain size is defined as indicated in Figure 3 and the boundary condition is defined accordingly in Table 2.

Table 2. Boundary and initial conditions.

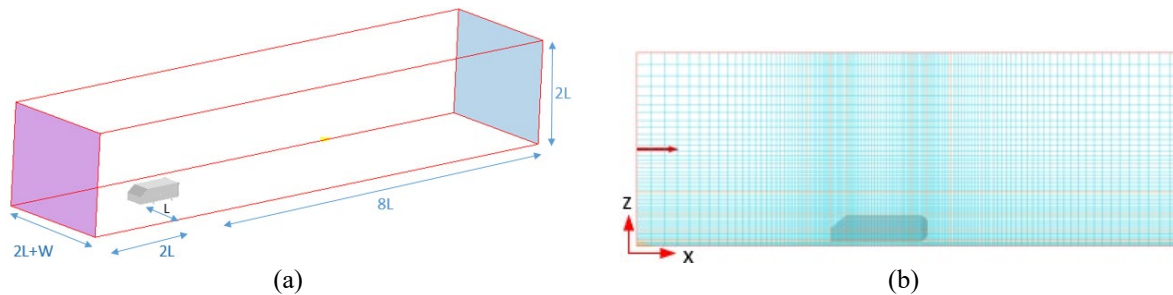| Boundary surface	Condition
Inlet	velocity boundary (60, 80, 100, 120km/h)
Outlet	pressure boundary
Sides and top	symmetric boundary
Ground	moving boundary with the same inlet velocity
Exterior surface	no slip condition with wall function
Interior (duct)	no slip condition with wall function
Flow field	quasi-3D, steady, turbulent and incompressible flow

Figure 3. (a) Numerical domain size and its (b) optimised grid (271×144×168).

Numerical grid dependence test was performed with C_D versus cells per million, as shown in Figure 4, and the optimum grid distribution is set as in Figure 3. With this setup, a numerical calculation has been done to see the aerodynamic effect of the air duct on drag force, rear flow and related flow property variations. The calculation was conducted at optimised grid distribution with different iteration number ranging from 5,000 to 10,000 and nicely converged with a cut off error ratio of the residual fraction less than 0.01%.
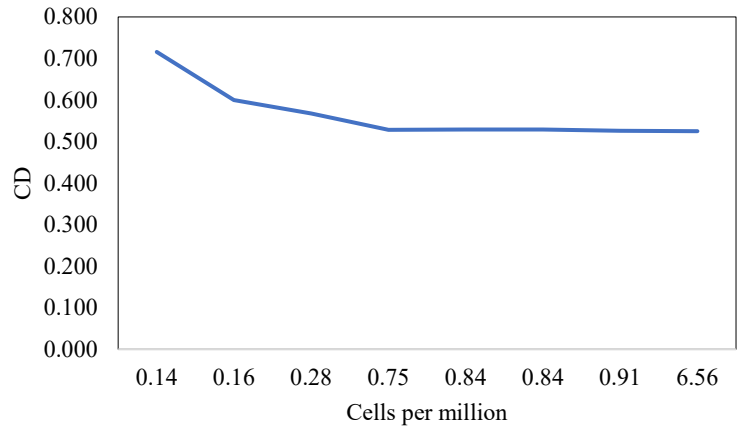
Figure 4. Grid dependence test.

Governing Equations

Three-dimensional governing equations for the numerical simulation of turbulent, incompressible and steady flow field are given below:

$$\frac{\partial U_i}{\partial x_i} + \frac{\partial U_j}{\partial y_i} + \frac{\partial U_k}{\partial z_i} = 0 \tag{4}$$

$$\frac{\partial}{\partial x_j}(U_i U_j) = -\frac{1}{\rho}\frac{\partial P}{\partial x_i} + \frac{\partial}{\partial x_j}\left[v\left(\frac{\partial U_i}{\partial x_j} + \frac{\partial U_j}{\partial x_i}\right) - \overline{u_i u_j}\right] - g_i \tag{5}$$

where: $-\overline{u_i u_j} = v_t\left(\frac{\partial U_i}{\partial x_j} + \frac{\partial U_j}{\partial x_i}\right) - \frac{2}{3}k\delta_{ij}, \qquad \delta_{ij} = 1 \;\; if \; i = j \;\; and \;\; \delta_{ij} = 0 \;\; if \; i \neq j$

Extended (κ-ε) closure turbulent model (KECHEN)

Turbulent kinetic energy equation:

$$\frac{\partial}{\partial x_i}(U_j k) = \frac{\partial}{\partial x_i}\left[\left(v + \frac{v_t}{\sigma_k}\right)\frac{\partial k}{\partial x_j}\right] + G - \varepsilon \tag{6}$$

wher $G = -\overline{u_i u_j}\frac{\partial U_i}{\partial x_j}$e [19, 20], $v_t = C_\mu \frac{k^2}{\varepsilon}$, $C_\mu = 0.09$

Energy dissipation equation:

$$\frac{\partial}{\partial x_i}(U_j \varepsilon) = \frac{\partial}{\partial x_i}\left[\left(v + \frac{v_t}{\sigma_\varepsilon}\right)\frac{\partial \varepsilon}{\partial x_j}\right] + \frac{\varepsilon}{k}(C_{\varepsilon 1}G) - C_{\varepsilon 2}\frac{\varepsilon^2}{k}) + C_{\varepsilon 3}f_1\frac{P_k^2}{K} \tag{7}$$

where, $C_\mu = 0.09$, $C_{\varepsilon 1} = 1.15$, $C_{\varepsilon 2} = 1.9$, $C_{\varepsilon 3} = 0.25$ $\sigma_k = 0.75$, $\sigma_\varepsilon = 1.15$ and f_1 is the Lam-Bremhorst (1981) damping function which tends to unity at high turbulence Reynolds numbers [21].

RESULTS AND DISCUSSION

This numerical study on a ducted vehicle model is conducted with a core objective to see the effect of an air duct on vehicle aerodynamic performance with an intention to improve electric vehicle energy economy. This could be possible in different ways. One of the options is improvement through aerodynamic drag reduction. The other alternative approach is harvesting aerodynamic energy by installing a harvesting unit in the duct. In addition, utilising the internal flow for battery cooling (thermal management application) which might be considered as spin-off activity of the first two approaches to improve energy efficiency. For these and other multiple benefits, understanding the flow characteristics of the air duct installed in the model vehicles and evaluating its effect on drag reduction is important. In this paper, the numerical result is discussed with a focus on the longitudinal duct flow characteristics and its effect on the drag forces of the modified simple body as preliminary research.

Duct Flow Characteristics

The ducts are made rectangular and through for basic research purpose as described under the model description section. The standard simple body used in this study is deliberately reverse oriented taking vans to shape for the sake of duct flow study and the slant angle acting as a front windshield. The test is conducted at four different speeds (60 km/h, 80 km/h, 100 km/h, and 120 km/h), but most of the result presented in this paper is obtained at 100km/h ($Re_{\_w} \approx 2.4 \times 10^6$) as a representative of other test conditions, and in some cases, the test speed is specified.

As the model moves with a given speed (flow speed), the upstream bulk fluid in front of the model decelerates and then stagnates at the object front vertical face due to the adverse pressure gradient. As portion of the front face is ducted, the fluid flow stream in line with the duct tends to continue flowing through duct. But, the flow deflection at the duct front entry edges due to the sharp corner being supplemented by the front flow stagnating vertical face is significantly impeding the duct flow. As a solution to minimise the flow convergence at the duct entry edges, chamfering technique (curved surfaces) are used at the duct front edges. Both results from models with and without chamfer are presented.

The in-duct flow velocity profile along the longitudinal (x-direction) at the middle of the duct is illustrated in Figure 5 for both ducts with and without chamfer for two ducted models M1 and M2, respectively. The velocity is normalised with the free stream velocity (U_∞), and the measuring point is normalised by the corresponding duct dimension (length).
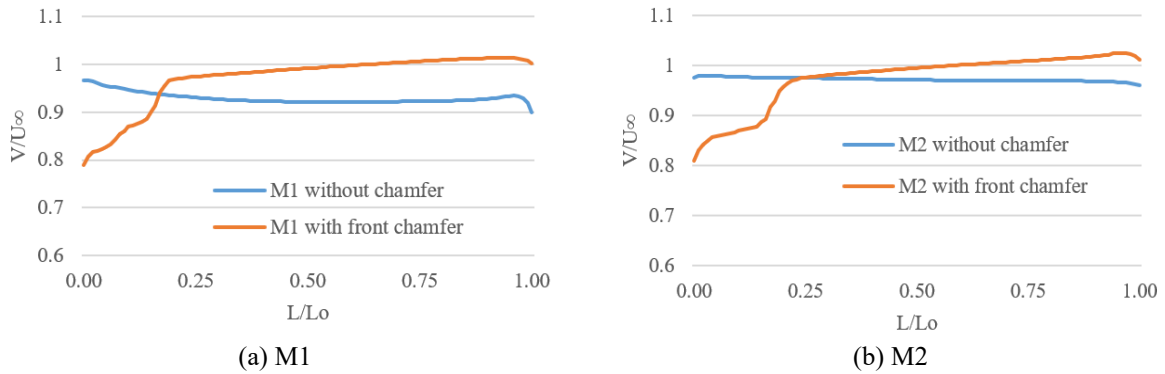

(a) M1   (b) M2

Figure 5. Comparison of the velocity distribution in the duct with and without front chamfer.

As shown in Figure 5, the in-duct flow can be divided into two flow regions. Entrance region which covers nearly first 25% in the duct front portion and the flow region in the remaining duct length. Both ducts flow behaves differently in both flow regions. In the duct without chamfer, the flow is not favoured at the entry because of the pinched flow cross-section caused by all four sharp entry edges, and this impedes the flow into the duct. Consequently, incoming flow shows deceleration tendency nearly in the whole duct flow region.

To the contrary, chamfering the duct entry edges minimised the flow convergence at the duct front edge and improved incoming flow. At the entrance region, a favourable pressure gradient accelerated the incoming flow together with the inertia force from the upstream flow. The flow accelerates rapidly after the duct entry edge in the first 25% of the duct region, gaining a momentum. Then, continue to accelerate gradually in the remaining flow region. Interestingly the velocity even becomes faster than the free stream velocity after about 60% of the longitudinal length of the duct.

The location of the inflection point presents important information for the placement of the turbine when considering energy harvest and about chamfer curvature optimisation. Similarly, the point where the flow speed exceeds the free stream velocity is important. Furthermore, accelerating the flow in the duct also has a great contribution to the concept of energy harvest and/or energy preservation. Of course, in addition to this simple technique (chamfering), other flow accelerating techniques need to be investigated or optimised for better duct flow acceleration taking in to account the internal flow influencing forces such as pressure, inertia and shear stress.

To further support the duct flow discussed above, duct pressure distribution and coefficient of pressure curve are also plotted. Figure 6 shows the pressure and coefficient of pressure variation along the longitudinal direction for the M1 model with and without chamfer. The curve for chamfered duct shows that the pressure drops rapidly at the entrance region of the duct and accelerating flow while the sharp-edged duct (without chamfer) relatively not favouring the incoming flow at the front edges and rather impeding the flow at the entry. In the case of the chamfered duct, as the flow goes on even after the entrance flow region, constant favourable pressure gradient ($\frac{dp}{dx}$ <0) is observed until near the duct exit where x is positive along the flow direction. At the exit, the pressure tends to rise adversely due to the flow resistance from the rear turbulent flow for a while and then the fluid flows out to merge with the rear wake. The result agrees with flow characteristics shown in Figure 5. The pressure coefficient (Cp) could be expressed as:

$$C_p = \frac{P - P_\infty}{q} \tag{8}$$

where P is static pressure at point of measurement, P∞ free stream pressure, and q is dynamic pressure based on the free stream velocity of the fluid.

Effect of Air Duct on Rear Flow

Ground vehicle as a bluff body, the rear flow structure is complicated due to the combined effect of the two trailing longitudinal vortices accompanied by 3D separation flow, the wake and eddies behind the rear base. It is known that the rear shape also influences the rear flow structure. Any flow control technique which could reduce the separation flow and reduce rear wake is believed to contribute to the drag reduction.

When air duct is applied to the vehicle model, one of the special effects observed at the rear flow is a momentum addition to the rear wake flow. This reduces the rear flow momentum loss, which causes recirculation behind the rear base and hence reduce rear pressure drag. The extent depends on the duct type, size, location and flow characteristic. In this study, only the ducts located at lower portions of the model are presented as described under model description section. Three different sizes of air ducts are used to illustrate the effect of the momentum added to the rear wake flow field in this section. The intension is to show the relative effect of duct and duct size on the rear wake cross-section at an arbitrary single location behind the model.
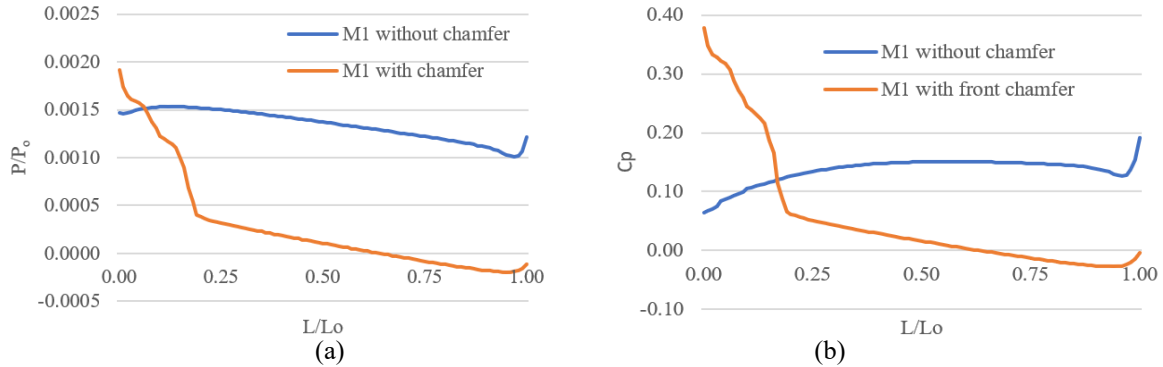
Figure 6. Comparison of the (a) pressure ratio (P/P_∞) and (b) pressure coefficient (Cp) distribution in the duct with and without front chamfer.

Velocity vector and contour plot of M2 and M3 are depicted in Figure 7, respectively at a plot plane of x = 0.2m (x=0.05Lo) from the rear edge of the model. It clearly indicates that the rear wake region is affected at the lower portion of the rear base by the flow jetted to the rear wake through the duct. On the model M3, it even tends to suppress the longitudinal trailing vortices and tried to merge into the single vortex at the rear centre slightly shifted to upper-middle. This momentum addition phenomenon has a significant impact on the pressure drag, and it is discussed more in the drag force section of this paper.
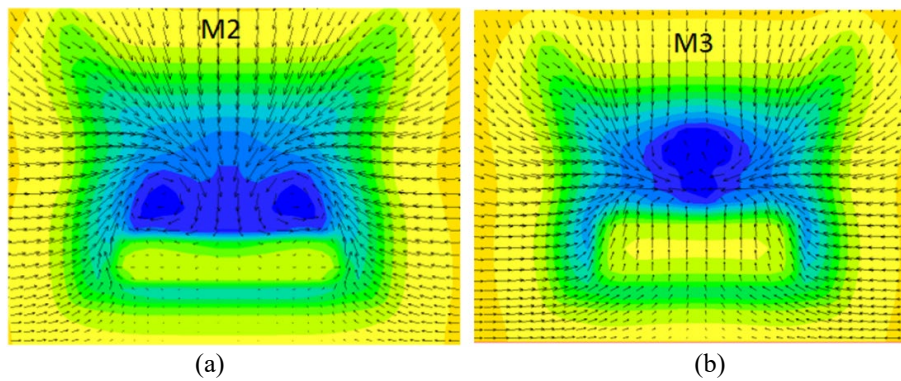

Figure 7. Velocity vector and contour plot of (a) M2 and (b) M3 at x = 0.2m (x=0.05Lo) from the rear edge of the model.

Figure 8 shows the change of the rear wake region with the air duct size. As shown in the contour plot, the wake cross-section at the specified location decreased with the bigger air duct size due to the linear momentum introduction into the rear flow region through the air duct.

Figure 9 shows the pressure contour plot of the rear side of M0 and M1 at the rear middle of the models (Z = 0.5H). M1 has a relatively wider and higher pressure region than M0. It means that M0 has lower pressure distribution than M1, and it is the cause of higher induced pressure drag of M0 than M1.
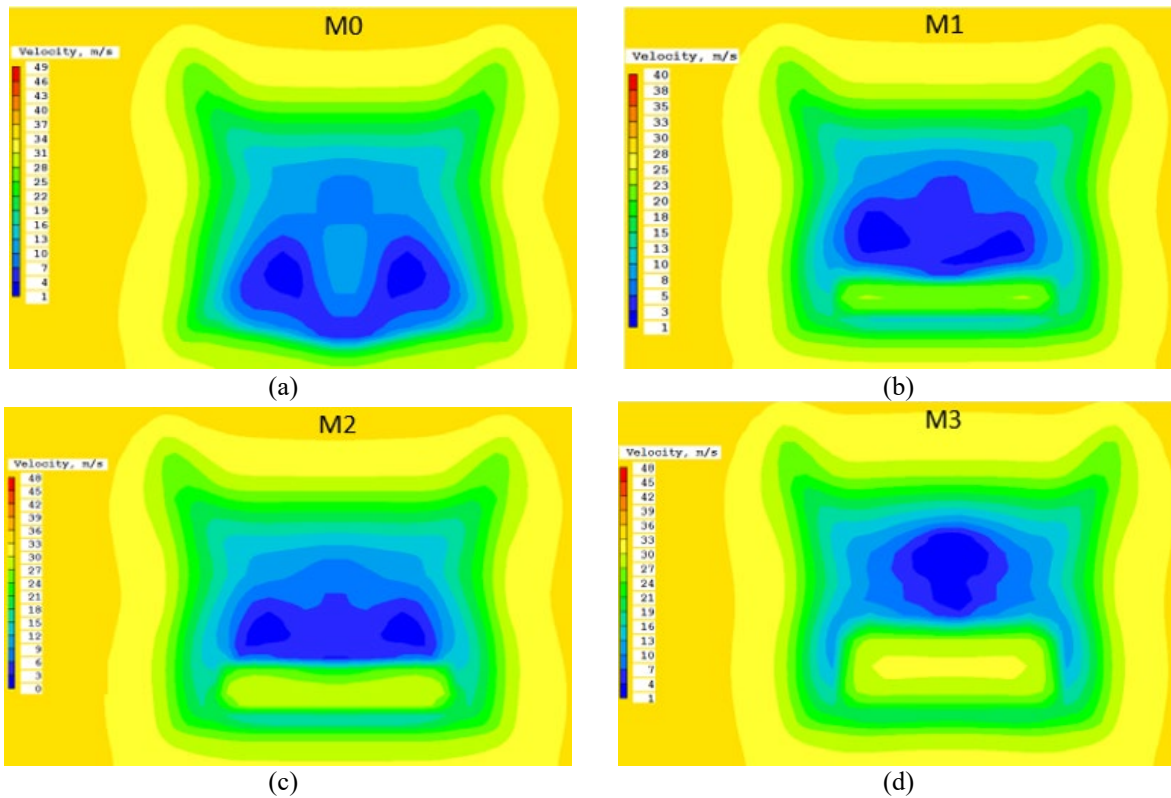
Figure 8. Comparison of the rear velocity contours of (a) M0, (b) M1, (c) M2 and (d) M3 at x=0.2 m in longitudinal direction from the rear edge of the air duct.

Figure 9. Comparison of the pressure contour of (a) M0 and (b) M1 at the rear flow region.

Duct Effect on the Drag Force

Pressure drags

The effect of the duct on the pressure drag is demonstrated qualitatively in Figure 10 using pressure and velocity contour plots of the model vehicles. Variation of the pressure intensity at the front and the rear of the model vehicle is clearly observed indicating the effect of the air duct. Therefore, the contribution of the duct to aerodynamic drag reduction is not only by acting as a control mechanism for the rear flow dynamics by the introduction of linear momentum to rear wake flow but also reducing the front stagnation pressure by preserving a portion of upstream flow kinetic energy.

As shown in the pressure contours, M2 shows the smallest stagnation pressure region in front and hence the lowest profile pressure drags among three models. At the rear region, M2 shows the higher pressure distribution due to the pressure recovery at the rear region. It means that the induced pressure drag at the rear also decreases due to the pressure recovery. All these flow phenomena in both vicinities of the vehicle body surely influence the variation of aerodynamic drag of the vehicle.

Figure 11 and 12 shows the change of front and rear pressure drag with the models at the moving speed. The higher pressure drag was observed on the base model M0 in both rear and front side. As the duct size increases the pressure drag decreases in both rear and front side. PHOENICS result file enables to evaluate pressure and friction drag forces acting on all six sides of the test model independently. For a typical model category with chamfered duct, about 19.5 % of the pressure drag reduction is observed in M1 when compared to M0. Out of this 10.1% reduction is from the front and the remaining 9.4% reduction is from the rear pressure drag of the model at 100km/h. For M2 from the same category, the pressure force reduction is about 26.6% of the total aerodynamic drag at the same speed. It means that the air duct has a very significant effect on the reduction of pressure drag of the bluff body under consideration.
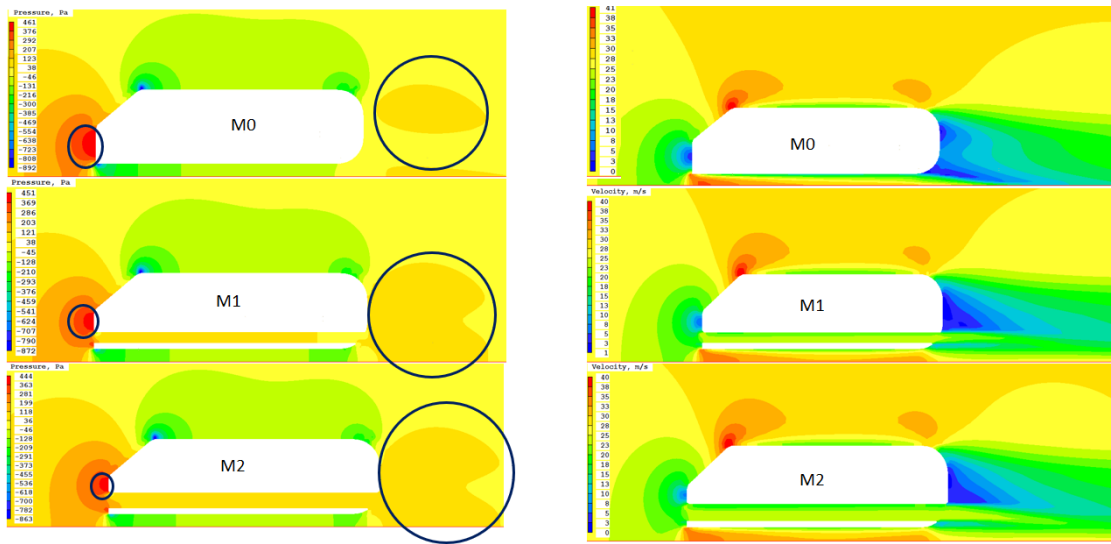
Figure 10. Comparison of the pressure and velocity contour plots of the model vehicles.
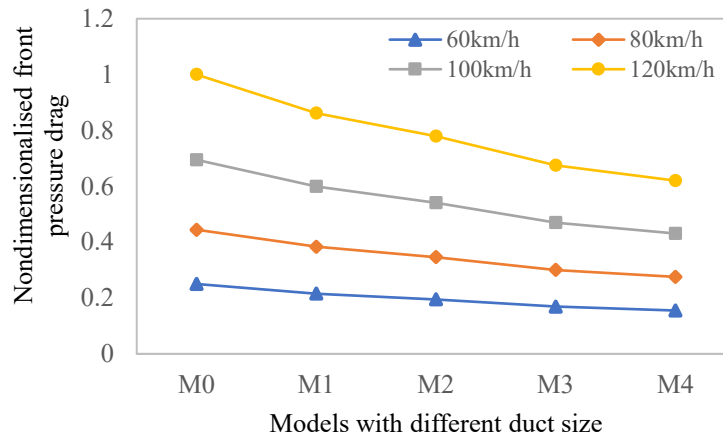

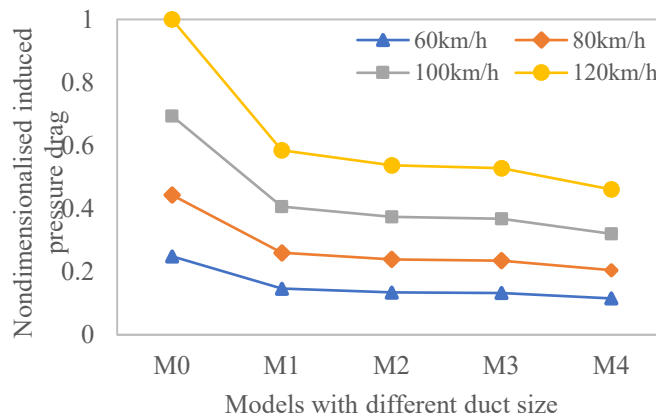**Figure 11.** Variation of the front pressure drag with the duct size at different speed

Figure 12. Variation of the induced pressure drag at the rear with the duct size at different speeds.

Skin friction drag

The friction drag is generated due to the viscous effect of air on the surface of the vehicle body. Even though the friction force is relatively small compared to pressure force on a ground vehicle, the air duct showed an adverse effect on the friction drag of the model. Figure 13 shows the variation of the friction drag to the duct size. It is found that the friction drag force of the ducted models is higher than M0 because of the increased surface area due to the air duct. The trend is similar for both ducted models with and without chamfer. As an illustration, in the case of M4 with the largest duct size with chamfer, the friction force increased about 4.28% of the total drag with respect to M0 at a speed of 100km/h specific test case.
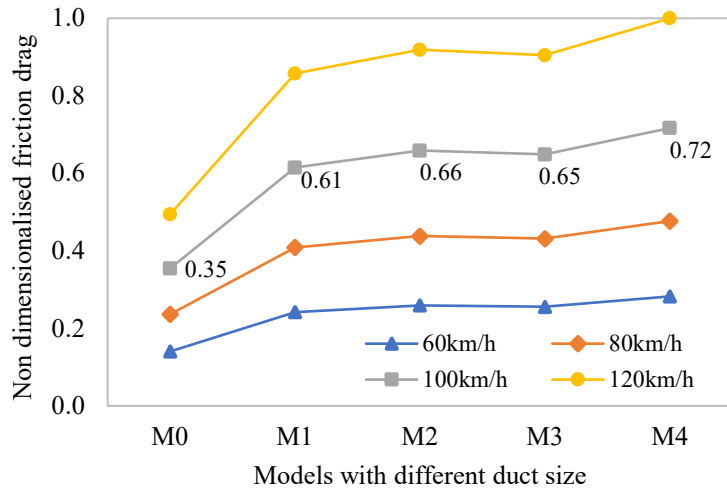
Figure 13. Variation of the friction drag with the duct size.

Total drag force

Figure 14 shows the total drag force of each vehicle model at 100km/h, which consists of friction and pressure drag for models without chamfer. The total drag of the model vehicle decreases with the increase of the air duct sizes, but the friction drags changes in reverse. Therefore, the total drag decreases significantly with the increase of the duct size due to the reduction of the stagnation pressure at the front side of the model vehicle and rear pressure recovery due to duct flow.
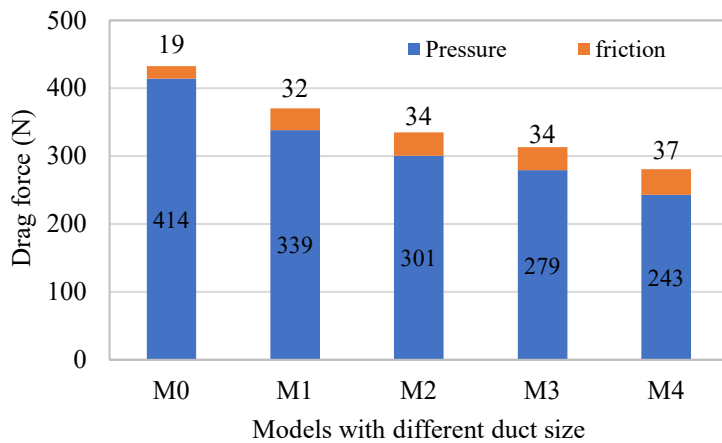

Figure 14. Variation of the total drag force with the duct size at 100km/h

Figure 15 shows the reduction of the total drag (in %) of the ducted Ahmed models without chamfer with respect to base model M0. The result indicates a significant decrease in the total drag force with the ducted Ahmed model vehicles. In the case of M4 without chamfer at a speed of 100km/h, the total drag is composed of about 13% friction drag and about 87% pressure drag. The total drag is decreased by about 35.3% of M0's.

Effect of Air Duct on other Aerodynamic Forces

Effect of ducting on static aerodynamic stability of the model is discussed in brief. Accordingly, with the assumption of levelled and straight road, without side wind, the ducted models exhibited less yaw and pitching moments showing better stability compared to the model without duct. The down forces showed slight increment. Therefore, the overall effect of the duct on the aerodynamic stability of the model can be considered as an affirmative contribution to the static stability of the model vehicle with the current configuration. The trend of yaw and pitching moment is shown in Figure 16 by non-dimensionalised values at a speed of 100 km/h. Both pitching and yawing moments of the ducted models is less than that of the base model (M0) without duct.
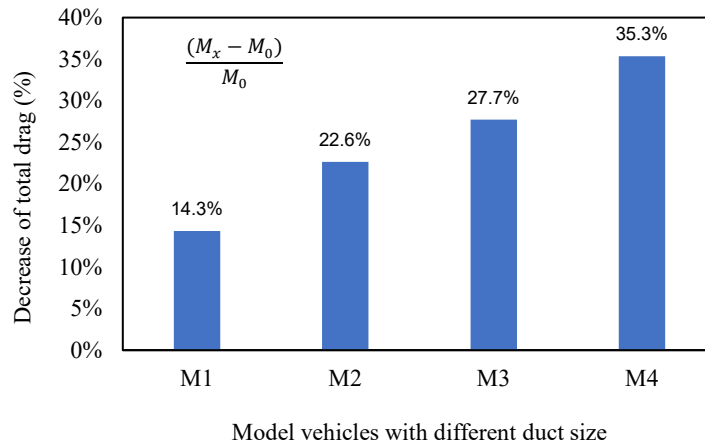
Figure 15. Increment of the total drag force of the ducted modes with M0 at 100 km/h.
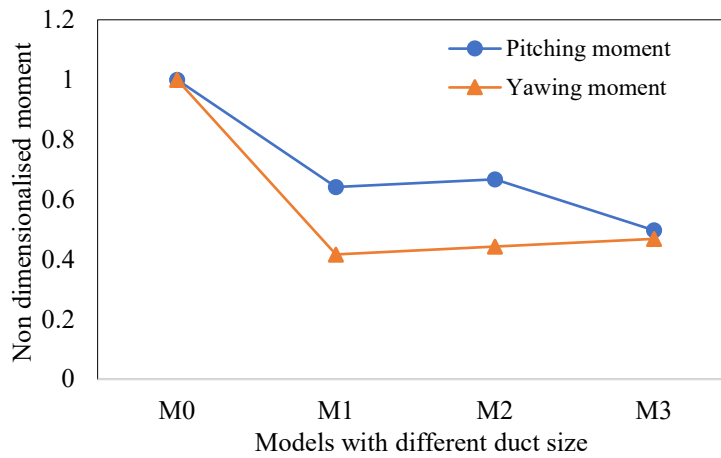

Figure 16. Yaw and pitching moment trend among models.

Furthermore, in all ducted models, the negative lift force showed an increase compared to the base model. A typical bar chart is shown in Figure 17. The trend is similar for both with and without chamfer. The increase in the downforce could favour for better traction. On the other hand, it could be considered as a side effect in increasing rolling resistance. But an important and interesting feature of the duct is its design flexibility in relation to vehicle stability forces. It gives a chance to even regulate or adjust down forces through duct design as required, and this is one of potential duct advantage observed during this research which makes the down forces manageable.
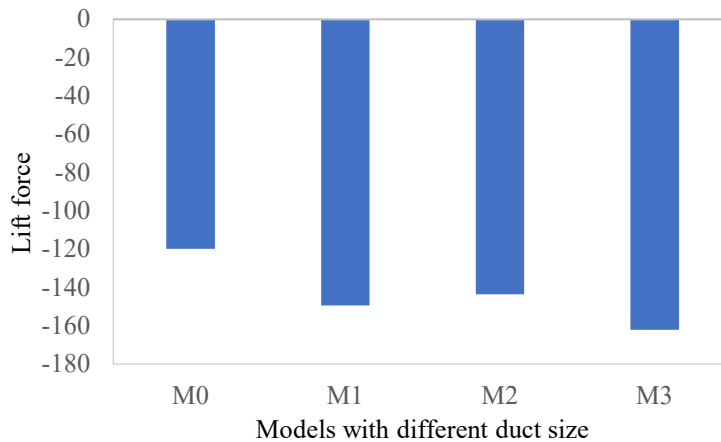

Figure 17. Lift forces (downforce) at 100 km/h for models with chamfer.

CONCLUSION

In this numerical study, the aerodynamic effect of the air duct installed in a simplified vehicle body was studied. A fundamental study on the effect of the air duct to improve the aerodynamic performance of an electric vehicle is

conducted. Basic flow analysis on fore-body, in-duct and rear flow are discussed in brief. For the details of the aerodynamic effect of the air duct on the model vehicle particularly on the front pressure drag, rear induced pressure drags, and the surface friction drag was analysed quantitatively. Effect of an air duct on the model stability forces is presented in brief.

Accordingly, the study showed that application of duct has a significant effect on the pressure drag reduction. To the contrary, the friction drags showed an increasing trend with duct size even though its effect on the total drag is less significant. Therefore, the ducted model vehicle had a significant reduction of the total aerodynamic drag compared to the unducted model vehicle. This aerodynamic drag reduction contributes to the energy savings of ground vehicle and extends the driving range of the vehicles with the given energy storage pack.

As an illustration of representative models, the model M1 without chamfered duct showed a pressure drag reduction of about 17.3% of the total drag, of which 10.1% is from the front pressure drag, and the remaining 7.2% reduction is from the rear pressure drag with respect to the base model Mo. To the contrary, the friction drag of this model is increased by about 3% of the total drag, that result in an overall drag reduction of 14.3%. Similarly, M1 with chamfered duct showed a pressure drag reduction of about 19.5% of the total drag, of which 10.1% is from the front side, and 9.4% is reduced from the rear pressure drag. At the same time, about 3.2% friction drag increase is observed, making the overall drag reduction of this chamfered model 16.3% of the total drag. This clearly illustrates the air duct effect on the aerodynamic drag of a vehicle where duct installation is suitable. Therefore, the advantage of an air duct on drag reduction and adverse effects of ducting on the aerodynamic flow is indicated.

Detailed experimental test and other extended applications of duct flow apart from drag reduction is part of the ongoing research. In general, based on this study, it is believed that ducting will open a new approach to improve energy economy of the ground vehicle either by reducing drag or by harvesting the flow kinetic energy where feasible. It is believed that the multiple purposes of ducting feature contribute a more extensive research topic to the field.

REFERENCES

[1]   Wood RM. Impact of Advanced Aerodynamic Technology on Transportation Energy Consumption. SAE World Congress 2004; 1–21.

[2]   Hucho WH, Sovran G. Aerodynamics of Road Vehicles. Annual Review of Fluid Mechanics 1993; 25: 485–537.

[3]   Hucho W. Aerodynamics of Road Vehicles: From fluid Mechanics to Vehicle Engineering. London: Butterworth-Heinemann Ltd, 1987.

[4]   Eun LC, Shakrine A, Rafie M, Wiriadidjaja S, Marzuki OF, An overview of passive and active drag reduction methods for bluff body of road vehicles. International Journal of Engineering &Technology 2018; 7(4.13): 53-56.

[5]   Hucho WH, Janssen LJ,.Emmelmann HJ. The optimisation of body details - a method for reducing the aerodynamic drag of road vehicles, SAE Technical paper: 760185;1976.

[6]   Altaf A, Omar AA, Asrar W, Review of passive drag reduction techniques for bluff road vehicles. IIUM Engineering Journal 2014; 15(1): 61–69.

[7]   Yunqing G, Tao L, Jiegang M, Zhengzan S, Peijian Z. Analysis of drag reduction methods and mechanisms of turbulent. Hindawi Applied Bionics and Biomechanics: 6858720; 2017.

[8]   Sudin MN, Abdullah MA, Shamsuddin SA, et al. Review of Research on Vehicles Aerodynamic Drag Reduction Methods. International Journal of Mechanical & Mechatronics Engineering 2014; 14: 35–47.

[9]   Kim C. A Streamlined Design of a High-Speed Coach for Fuel Savings and Reduction of Carbon Dioxide. International Journal of Automotive engineering(Japan) 2011; 2: 101–107.

[10]   Nalanagula S, Varadharajan GT. Aerodynamics drag reductions methodology for the commercial vehicles using computational Fluid dynamics. SAE Technical Paper: 2016-01-8139; 2016.

[11]   McCallen RC et al. DOE's effort to reduce truck aerodynamic drag - joint experiments and computations lead to smart design. In: 34th AIAA Fluid Dynamics Conference and Exhibition, Portland, United States, pp. 1–16, 2004.

[12]   McCallen R et al., Progress in reducing aerodynamic drag for higher efficiency of heavy duty trucks (class 7-8). SAE Technical paper: 1999-01-2238; 1999.

[13]   Altinisik A, Yemenici O, Umur H. Aerodynamic analysis of a passenger car at yaw angle and two-vehicle platoon. Journal of Fluids Engineering 2015; 137(12):121107.

[14]   Johnson TV. Review of Vehicular Emissions Trends. SAE International Journal of Engines 2015; 8: 2015-01–0993.

[15]   Ehsani M, Gao Y, Gay SE, et al. Modern Electric, Hybrid Electric, and Fuel Cell Vehicles. second edi. CRC Press, 2005.

[16]   Heft AI, Indinger T, Adams NA. Introduction of a New Realistic Generic Car Model for Aerodynamic Investigations. SAE International 2012; 1–14.

[17]   Ahmed SR, G.Ramm, G.Faltin. Some Salient Features of the Time -Averaged Ground Vehicle Wake. SAE Transaction 1984; 93: 473–503.

[18]   Chen YS and Kim SW. Computation of Turbulent Flows Using an Extended K-Epsilon Turbulence Closure Interim Report. Alabama, 1987.

[19]   Tennekes H. A first course in turbulence. Massachusetts: The MIT Press, 1972.

[20]   Ferzinger HJ, Peric M. Computational methods for fluid dynamics. 3rd ed. Springer publishing group, 2002.

[21]   Banks J, Turbulence modeling in PHOENICS, 2007.Retrieved from http://www.cham.co.uk/phoenics/d_polis/d_enc/turmod/enc_t342.htm.; 3 December, 2019